METALLURGY

Ultrauniform, strong, and ductile 3D-printed titanium alloy through bifunctional alloy design

Jingqi Zhang[1]†, Michael J. Bermingham[1]†, Joseph Otte[2], Yingang Liu[1], Ziyong Hou[3,4,5], Nan Yang[1], Yu Yin[1], Mohamad Bayat[6], Weikang Lin[1], Xiaoxu Huang[3,4], David H. StJohn[1], Matthew S. Dargusch[1]*

Coarse columnar grains and heterogeneously distributed phases commonly form in metallic alloys produced by three-dimensional (3D) printing and are often considered undesirable because they can impart nonuniform and inferior mechanical properties. We demonstrate a design strategy to unlock consistent and enhanced properties directly from 3D printing. Using Ti−5Al−5Mo−5V−3Cr as a model alloy, we show that adding molybdenum (Mo) nanoparticles promotes grain refinement during solidification and suppresses the formation of phase heterogeneities during solid-state thermal cycling. The microstructural change because of the bifunctional additive results in uniform mechanical properties and simultaneous enhancement of both strength and ductility. We demonstrate how this alloy can be modified by a single component to address unfavorable microstructures, providing a pathway to achieve desirable mechanical characteristics directly from 3D printing.

T hree-dimensional (3D) printing or additive manufacturing (AM) of metals and alloys typically involves multiple physical and metallurgical phenomena that impart complex microstructures and varied mechanical properties in the fabricated products (1–7). For metallic alloys, which solidify with a cubic crystal structure, columnar grains often prevail in the 3D-printed part (8, 9) because grains with the easy growth <100> directions tend to align closely to the maximum temperature gradient of the melt pool and grow epitaxially from the partially melted layers (10). Although this highly textured columnar grain structure can be beneficial for certain applications, in most cases it is undesirable because it degrades the mechanical performance and results in mechanical property anisotropy (11, 12). Accordingly, extensive effort has been devoted to transforming the coarse columnar grain structure into fine equiaxed grains to achieve superior and isotropic mechanical properties (13–17). Generally, the columnar-to-equiaxed transition (CET) and grain refinement can be promoted through process control and by adding grain-refining inoculants (12, 18). The former typically includes manipulating the 3D printing processing parameters or introducing external interferences (16, 17). However, the effectiveness and practicalities of this approach are limited to specific alloys or 3D printing technologies.

Alternatively, the metallurgical approach through additives has proven highly effective but often results in an undesirable loss in ductility owing to the formation of brittle second phases (9). Therefore, simultaneously addressing the coarse columnar grains and eliminating property anisotropy without adversely affecting the ductility is highly desirable.

A further complication is that many allotropic alloy systems, including titanium alloys, are also susceptible to the heterogeneous distribution of phases associated with the solid-state thermal cycling experienced during the 3D printing process (19–22). This poses an additional challenge to achieve uniform mechanical properties of 3D-printed parts made from these alloys (23, 24). The localized heating, cooling, and reheating nature of 3D printing effectively creates dynamic in situ heat treatments that encourage the decomposition of initially formed phases and/or the precipitation of new phases through solid-state phase transformations (20, 25). Because thermal cycles are spatially variable, the associated heat treatments can produce an inhomogeneous distribution of phase along the building direction of the part, thereby resulting in the spatial variation of mechanical properties (21, 22). Postprinting heat treatments can be effective in mitigating these phase heterogeneities but introduce delays and additional costs and are not effective in refining textured columnar grains (26). The confluence of these issues has made it extremely challenging to achieve uniform and superior mechanical properties in the as-fabricated state.

We demonstrate a design strategy to address this challenge by simultaneously controlling the grain structure and constituent phases in products manufactured by laser powder bed fusion (L-PBF). We selected the Ti−5Al−5Mo−5V−3Cr (Ti-5553) metastable β titanium alloy as a model alloy because it shows the coex-istence of coarse columnar β grains and a heterogeneous distribution of phases (Fig. 1, A to C). This results in highly nonuniform, position-dependent tensile properties from L-PBF, as we demonstrate (Fig. 1, D and E) and as has been demonstrated in other studies across multiple 3D printing technologies (27–29). We show that the single addition (up to 5.0 wt %) of elements from the β-isomorphous group [in this case, we selected Mo; see section on alloy design in the materials and methods (30)] into Ti-5553 powder to form a composite blend achieves bifunctionality: (i) During 3D printing, some of the Mo particles partially melt, but the core survives to nucleate fine grains during solidification and prevent coarse columnar grains from forming. (ii) The dissolved Mo solute stabilizes the β phase and suppresses the formation of isothermal ω phases and α phases under solid-state thermal cycling. As a result, the microstructural change because of the bifunctional Mo addition not only results in an improved uniformity in mechanical properties, but simultaneously enhances the strength and ductility. In general, the design strategy provides a pathway for achieving uniform and enhanced mechanical properties in parts produced by 3D printing.

Mechanical properties

We added 2.5 wt % and 5.0 wt % Mo to Ti-5553 (which we refer to as Ti-5553+2.5Mo and Ti-5553+5Mo, respectively) by mechanical mixing and produced the Ti-5553 parts with and without Mo additions using refined L-PBF processing parameters for titanium alloys (30). Given the fact that the part dimension and size can affect the thermal history and consequently the mechanical properties of the part (31), we adopted two types of part geometries (dog-bone– and cuboid-shaped parts; fig. S2) to evaluate the effect of Mo additions on mechanical properties. For simplicity, we discuss the representative data of Ti-5553+5Mo unless otherwise stated. We compare the tensile engineering stress-strain curves of Ti-5553 and Ti-5553+5Mo specimens (Fig. 2A), which were machined from the cuboid parts. In marked contrast to Ti-5553, which exhibits inferior tensile properties and substantial property variation throughout the parts, Ti-5553+5Mo shows enhanced and more uniform mechanical properties (see fig. S3 for fracture analysis). We also found the high consistency in mechanical properties of Ti-5553+5Mo in the dog-bone–shaped parts (fig. S4), regardless of the change in part geometry. To evaluate the degree of anisotropy of the tensile ductility, we compared the tensile ductility data of Ti-5553+5Mo with those of Ti-5553 and similar alloys that have a small deviation from the chemical composition of Ti-5553—that is, Ti−5Al−5Mo−5V−3Cr−1Zr (Ti-55531) and Ti−5Al−5Mo−5V−1Cr−1Fe (Ti-55511) (Fig. 2B) (27, 28, 32–34). Generally, a substantial deviation of the ductility data point from the blue dashed

[1]School of Mechanical and Mining Engineering, The University of Queensland, St. Lucia, Brisbane, QLD, Australia. [2]Centre for Microscopy and Microanalysis, The University of Queensland, St. Lucia, Brisbane, QLD, Australia. [3]International Joint Laboratory for Light Alloys (Ministry of Education), College of Materials Science and Engineering, Chongqing University, Chongqing, China. [4]Shenyang National Laboratory for Materials Science, Chongqing University, Chongqing, China. [5]Department of Materials Science and Engineering, KTH Royal Institute of Technology, Stockholm, Sweden. [6]Department of Mechanical Engineering, Technical University of Denmark, Lyngby, Denmark.
*Corresponding author. Email: m.dargusch@uq.edu.au
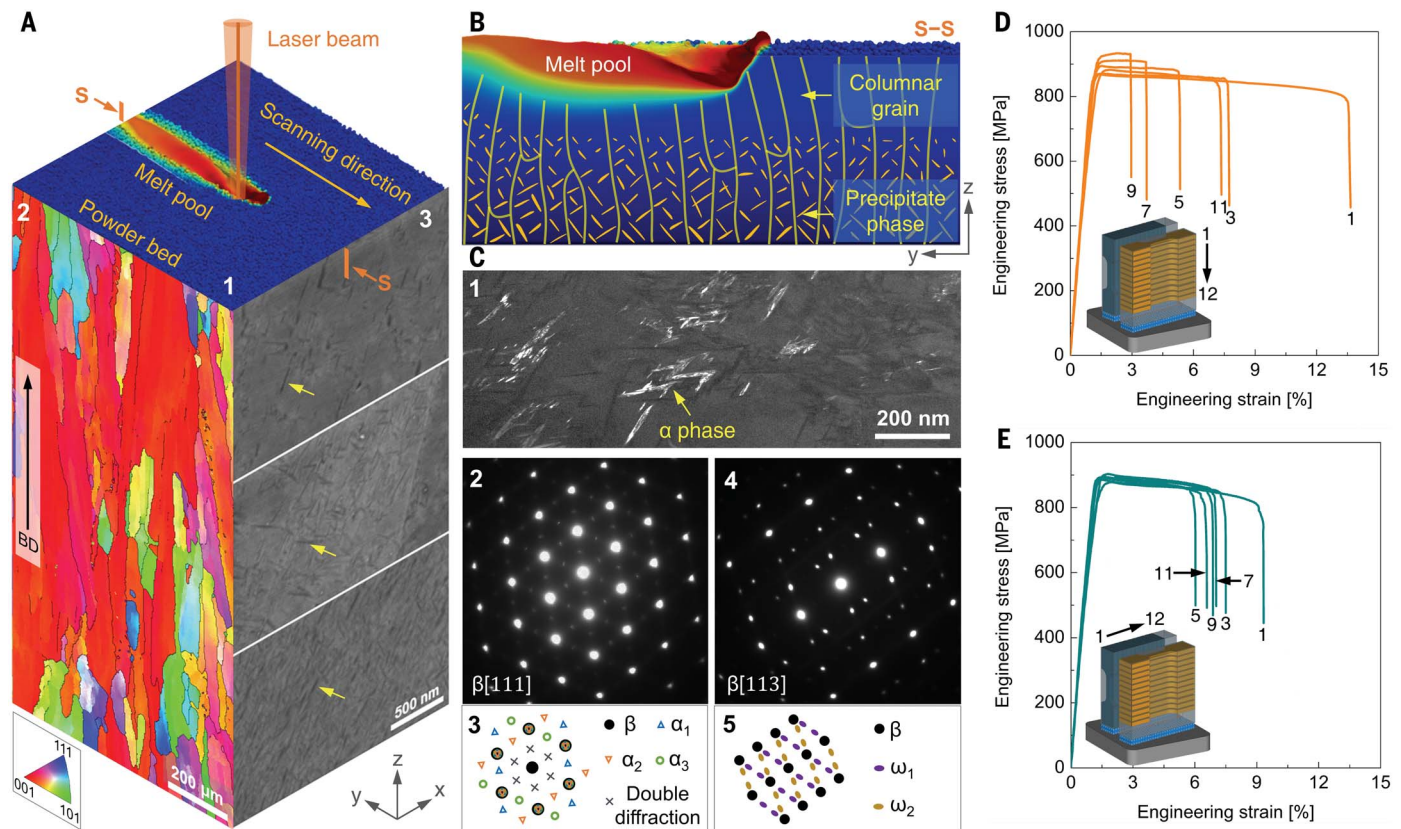†These authors contributed equally to this work.

Fig. 1. Microstructures and mechanical properties of Ti-5553 produced by L-PBF. (**A**) The coexistence of coarse columnar β grains and spatially dependent phases in Ti-5553 produced by L-PBF. (1) Schematic illustration of the L-PBF process. (2) EBSD IPF map showing coarse columnar β grains along the building direction (BD). (3) SEM-BSE micrographs showing the phase distribution along the BD. The yellow arrows point out α phases with a darker contrast in the β-Ti matrix. (**B**) Schematic illustration of the microstructure heterogeneity in terms of columnar β grains and heterogeneously distributed phases on the cross-section S–S (the yz-plane), as indicated in (A). (**C**) TEM micrographs of Ti-5553. (1) Dark-field TEM image showing α phases. (2) TEM SAED pattern from the [111]β zone axis showing the presence of α phases. The key diagram of the diffraction is shown in (3). Note that there are three α variants with the same zone axis of [$2\bar{1}\bar{1}0$], which grow in different directions. (4) TEM SAED from the [113]β zone axis showing the existence of isothermal ω phases. The key diagram of the diffraction is shown in (5). Note that there are two ω variants. (**D**) Tensile engineering stress-strain curves of Ti-5553 horizontal tensile specimens (1, 3, 5, 7, 9, and 11). The inset shows how the horizontal tensile specimens were machined from the Ti-5553 part. (**E**) Tensile engineering stress-strain curves of Ti-5553 vertical tensile specimens (1, 3, 5, 7, 9, and 11). The inset shows how the vertical tensile specimens were machined from the Ti-5553 part.

line indicates a high degree of anisotropy in the tensile ductility. Ti-5553+5Mo clearly shows higher and more isotropic ductility compared with Ti-5553 and similar alloys.

We also compared the yield strength and the elongation to failure of Ti-5553+5Mo with those of Ti-5553 (as well as those of Ti-55531 and Ti55511) produced in the as-fabricated L-PBF state and under postprinting heat treatment conditions (Fig. 2C) (*29, 32, 34–38*). Compared with Ti-5553 and its similar alloys in the as-fabricated state, Ti-5553+5Mo shows comparable yield strength but notably higher ductility. Postprinting heat treatment is commonly used to balance the mechanical properties of Ti-5553 produced by L-PBF. Although a high yield strength (>1100 MPa) can be achieved under certain heat treatment conditions, the ductility often deteriorates substantially, with an elongation to failure of <10%, which limits the use in safety-critical applications. For exam-

ple, a minimum elongation to failure of 10% is recommended for the use of Ti–6Al–4V, which is the so-called workhorse in the titanium industry (*20*). By contrast, without the need for downstream heat treatments, Ti-5553+5Mo shows an excellent balance of strength and ductility directly from L-PBF, which makes it stand out from Ti-5553 and the associated similar alloys in the strength-ductility map.

Grain structures

The exceptionally uniform and enhanced mechanical properties of Ti-5553+5Mo relative to Ti-5553 require a careful examination of microstructures and the associated underlying mechanisms. We first performed microfocus computed tomography (micro-CT) of Ti-5553 and Ti-5553+5Mo to evaluate the part quality. Overall, both Ti-5553 and Ti-5553+5Mo show a very high density, with total pore volume fractions of 0.004024% and 0.001589%, respectively

(fig. S5 and table S1). Such a high density indicates that porosity is unlikely to be responsible for the highly scattered tensile properties of Ti-5333 (Fig. 1, D and E) and is also in line with the high consistency in mechanical performance of Ti-5553+5Mo (Fig. 2A).

To reveal the effect of Mo additions on the grain structure, we carried out electron backscatter diffraction (EBSD) characterization of Ti-5553 and Mo-doped Ti-5553 (Fig. 3; the EBSD maps of Ti-5553+2.5Mo are provided in fig. S6). The microstructures of Ti-5553 consist of relatively large grains along the scanning direction (Fig. 3A, panel 1) and coarse columnar β grains along the building direction (Fig. 3A, panel 2), which exhibit strong crystallographic textures (fig. S7A). The addition of 5.0 wt % Mo to Ti-5553 results in a notable change in the grain structure and associated crystallographic texture. Numerous fine equiaxed grains (~20 μm in diameter) are evident, forming along the edges
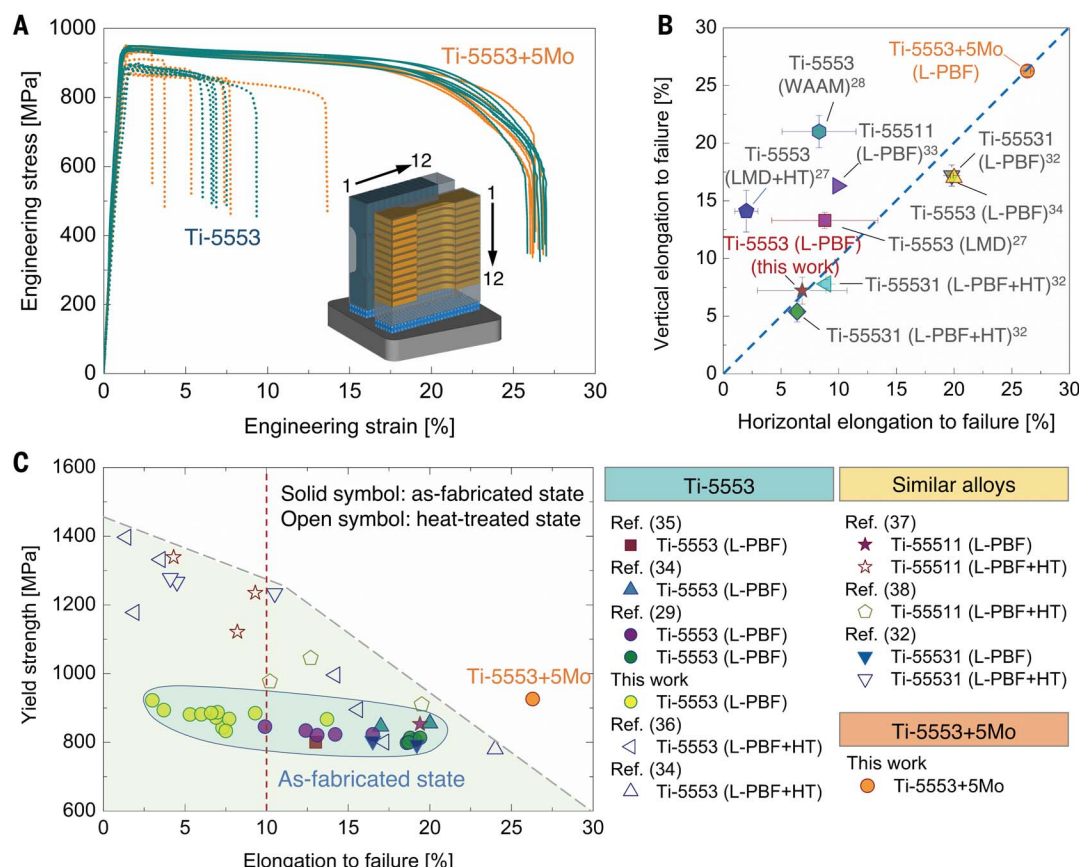
Fig. 2. Mechanical properties of Ti-5553 and Ti-5553+5Mo produced by L-PBF. (**A**) Tensile engineering stress-strain curves of Ti-5553 and Ti-5553+5Mo specimens, which were machined from the cuboid parts (as shown in the inset). Note that the tensile curves of Ti-5553+5Mo are from the selected tensile specimens (1, 3, 5, 7, 9, and 11), which are the same as Ti-5553 as shown in Fig. 1, D and E. (**B**) Comparison of the vertical and horizontal elongation with failure of Ti-5553, Ti-55531, Ti-55511, and Ti-5553+5Mo produced by multiple 3D printing technologies with and without postprinting heat treatment (HT). Error bars represent the standard deviation of the elongation to failure, but some are smaller than the size of the data symbols. LMD, laser metal deposition; WAAM, wire arc additive manufacturing. (**C**) Comparison of the tensile properties of Ti-5553+5Mo with those of Ti-5553, Ti-55531, and Ti-55511 in both as-built L-PBF and heat-treated states.

of scanning tracks of Ti-5553+5Mo (Fig. 3B, panel 1). By contrast, the microstructure of Ti-5553+5Mo is characterized by fine equiaxed grains and narrow columnar grains along the building direction (Fig. 3B, panel 2). Close examination of the microstructure reveals a periodic distribution of fine and columnar grains. Unlike in Ti-5553, where the highly textured columnar grains span across multiple layers, the length scale of columnar grains in Ti-5553+5Mo is determined by the melt pool size, and the crystallographic texture becomes random and weak (fig. S7B).

During solidification, the segregating alloy solute can restrict the growth of the solid phase by generating constitutional supercooling (ΔT_{CS}), which plays a key role in promoting the CET and grain refinement (39, 40). Two parameters are often used to provide an indication of how likely a solute is to generate constitutional supercooling and promote the CET. The first is the growth restriction factor Q, which represents the initial rate that ΔT_{CS} develops. The second is the freezing range (ΔT_{FR}), also known

as the supercooling parameter, which represents the maximum possible ΔT_{CS} that can develop (41). Despite being heavily alloyed, Ti-5553 contains alloying elements Al, Mo, V, and Cr, which show rather limited constitutional supercooling (in terms of Q and ΔT_{FR}) in titanium (18). The total Q and ΔT_{FR} values based on the real chemical composition of Ti-5553 are calculated to be about 10.4 K and 10.9 K, respectively (30) (table S3). These values are far below those reported in other studies to achieve substantial grain refinement by solute—for example, Q = 62 K and ΔT_{FR} = 603 K in Ti–8.5Cu (9, 42). Therefore, it is unsurprising that the L-PBF–produced Ti-5553 shows the typical columnar grain structure (Fig. 3A). The addition of Mo (2.5 wt % and 5.0 wt %) to Ti-5553 results in a pronounced change in the grain structure (Fig. 3B and fig. S6). Such a notable microstructural change could not be primarily attributed to the generation of constitutional supercooling because the Mo addition up to 5.0 wt % results in maximum total alloy Q and ΔT_{FR} values of 12.5 K and 12.8 K, respectively

(table S3), which assumes that all of the added Mo particles have fully dissolved in the titanium matrix. However, a dense population of residual Mo particles exists in the microstructure (fig. S5, D and E), which indicates incomplete dissolution of the added Mo particles. Despite the apparent lack of Mo solute toward ΔT_{CS}, the transient nature of Mo particle dissolution and potential higher local concentration around the particles (>5.0 wt % Mo) may generate further constitutional supercooling and help contribute toward the grain refinement in concert with other mechanisms.

Mo-rich particles

To gain a deeper insight into the role of Mo addition in solidification, we then focused on the topmost layers of Ti-5553 and Ti-5553+5Mo. Unlike the lower region of the fabricated part, where the microstructure can be substantially altered owing to the deposition of subsequent layers, the topmost layer only undergoes one or several thermal cycles because of the deposition of neighboring tracks. In principle, such
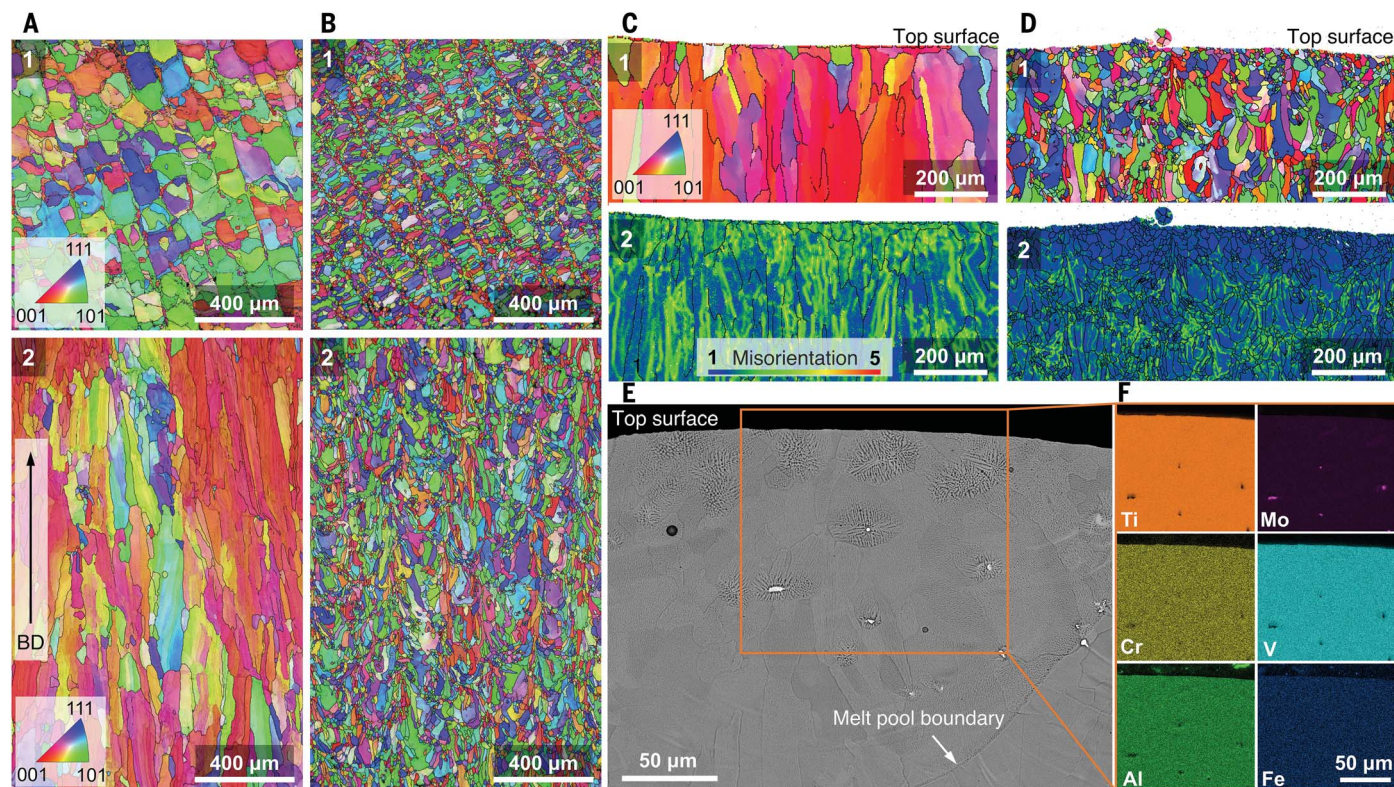
Fig. 3. Microstructure characterization of Ti-5553 and Ti-5553+5Mo.
(**A**) EBSD IPF maps (overlaid with the image quality map and high-angle grain boundaries with the misorientation angle ≥10°) of the xy-plane (along the scanning direction) (1) and the xz-plane (along the building direction) (2) of the Ti-5553 sample. (**B**) EBSD IPF maps (overlaid with image quality map and high-angle grain boundaries with the misorientation angle ≥10°) of the xy-plane (1) and xz-plane (2) of the Ti-5553+5Mo sample. (**C**) EBSD maps of the top surface layers of Ti-5553. (1) IPF map overlaid with high-angle grain boundaries. (2) KAM map. (**D**) EBSD maps of the top surface layers of Ti-5553+5Mo. (1) IPF map overlaid with high-angle grain boundaries. (2) KAM map. (**E**) SEM-BSE micrograph of the top surface of Ti-5553+5Mo. (**F**) SEM-EDX maps showing the elemental distribution in the region in (E).

thermal cycling is much weaker compared with that experienced by the lower region, and hence the topmost layer can provide a window for understanding the role of Mo in solidification. We show the EBSD inverse pole figure (IPF) and kernel average misorientation (KAM) maps of the microstructure close to the top surfaces of Ti-5553 (Fig. 3C) and Ti-5553+5Mo (Fig. 3D), respectively. Ti-5553 exhibits coarse columnar grains in the upper layer (Fig. 3C), whereas Ti-5553+5Mo is dominated by fine equiaxed grains (Fig. 3D). Further characterization of Ti-5553+5Mo by scanning electron microscopy (SEM)–backscattered electrons (BSE) shows that there are some particles located at the center of the equiaxed dendrite grains (Fig. 3E and fig. S8), which is a typical characteristic of a nucleating particle seeding a grain. Such particles are enriched in Mo, as evidenced by SEM–energy-dispersive x-ray spectroscopy (EDX) mapping (Fig. 3F).

To further explore these Mo-rich particles, we performed SEM-EDX and transmission electron microscopy (TEM)–EDX line-scanning across the interface between the Mo-rich particles and the titanium matrix (fig. S9 and Fig. 4A). The concentration profile obtained using SEM-EDX shows that there is a gradual change from the Mo particle to the titanium matrix (fig. S9, B to D), which is also confirmed by TEM-EDX line-scanning (Fig. 4B). Additionally, the high-resolution TEM imaging shows that the Mo-rich particle matches perfectly with the titanium matrix with a coherent interface (Fig. 4C).

Our SEM and TEM observations suggest that the transitional region across the Mo particle and titanium matrix plays an important role in grain refinement. Because these characterizations were performed on the samples that have undergone both solidification and solid-state transformations during L-PBF, it remains unclear whether the transitional region at the interface develops in the melt pool or results from solid-state diffusion after solidification. Unfortunately, this process cannot readily be characterized by current experimental techniques. To help understand the dissolution of Mo particles during solidification, we performed diffusion simulation using DICTRA (diffusion-controlled transformation) (Fig. 4D). The simulation is based on the assumption that an individual Mo particle with a radius of 2.5 μm is presented in the Ti-5553 melt pool (with a simulation cell of 100 μm) and then evolves during the heating and the subsequent cooling

processes before solidification. It is evident that during the heating process (from time = 0 s to time = 7.68×10^{-4} s) and the cooling process (from time = 7.68×10^{-4} s to time = 1.54×10^{-3} s), significant diffusion of Mo solute from the Mo particle to the Ti-5553 melt leads to a Mo-rich region surrounding the particle. Careful examination of the composition profiles of Mo in the DICTRA simulation and the SEM-EDX characterization reveals that the dissolution region from simulation is slightly larger than that from experimental characterization. This observation can be explained by the fact that, under realistic conditions, the fluid flow within the melt pool encourages the Mo-rich solute to rapidly diffuse and mix with the bulk liquid, thereby leading to a narrower Mo-rich region. Nevertheless, the DICTRA simulation supports our hypothesis that the transitional region across the Mo particle and titanium matrix can occur during the moments before and during solidification, although it would be further facilitated by subsequent solid-state diffusion during cooling after solidification.

On the basis of the experimental and simulation results, it appears clear that the contribution of Mo additions to grain refinement
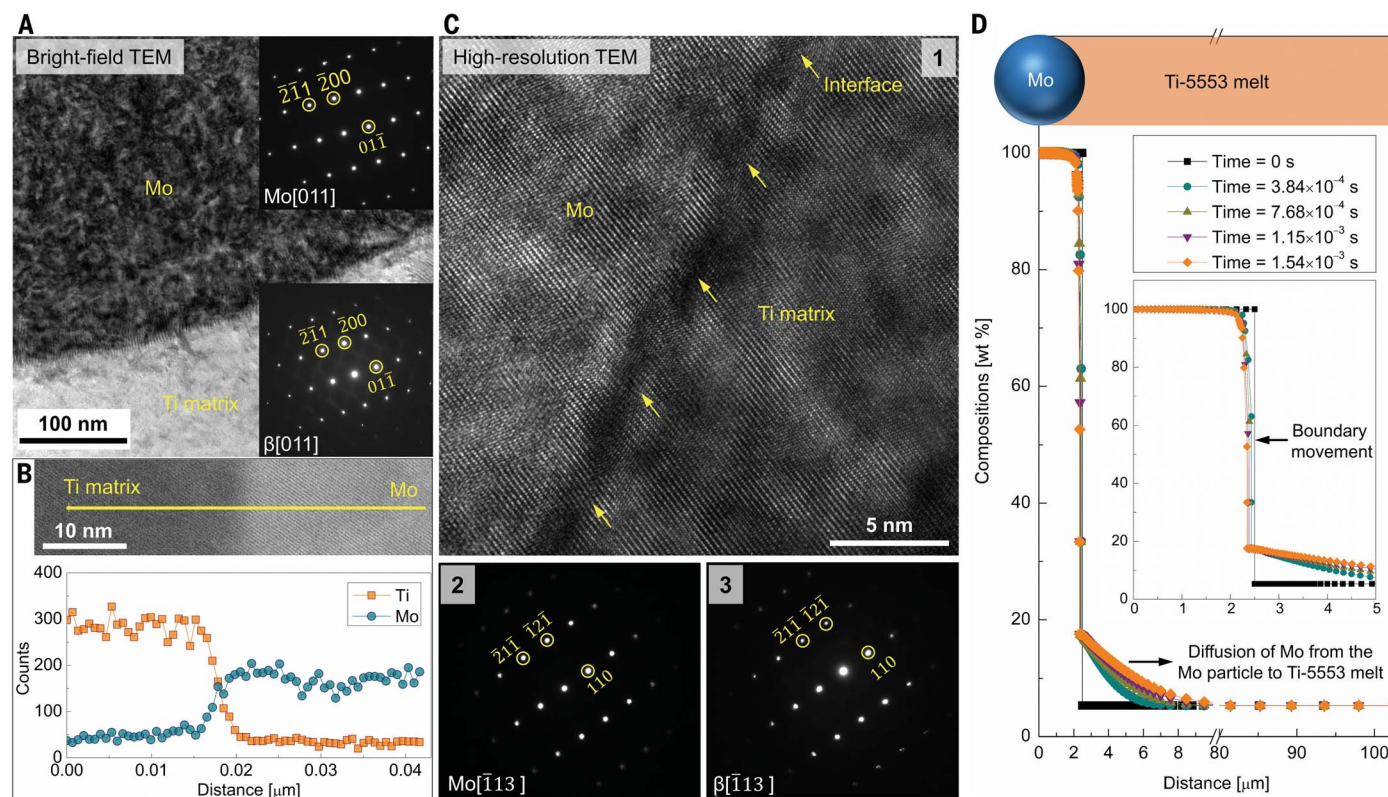
Fig. 4. TEM characterization and DICTRA simulation of the interface between Mo particles and the titanium matrix. (**A**) Bright-field TEM micrograph showing the interface of a Mo particle and the titanium matrix. Insets show the SAEDs from the [011] zone axis of Mo and β-Ti. (**B**) TEM-EDX line-scanning showing the compositional profile across the interface of the Mo particle and titanium matrix. (**C**) High-resolution TEM (HRTEM) image showing the coherent interface between the Mo particle and titanium matrix (1), along with the SAEDs of Mo (2) and Ti matrix (3) taken from the [$\bar{1}$13] zone axis. (**D**) DICTRA simulation showing the diffusion across the Mo particle and titanium melt during the heating and cooling processes of L-PBF. The inset shows a higher magnification of the composition profile of Mo and the boundary movement resulting from the dissolution process.

works in two ways: (i) The solid cores that survive in partially dissolved Mo particles act as heterogeneous nucleation sites for the new grains. (ii) The Mo solute associated with the dissolution of Mo particles surrounding the solid core potentially generates a supercooled region that enhances heterogeneous nucleation efficiency of the partially melted Mo particles. We schematically illustrate the mechanism of grain refinement in fig. S10. Upon being heated to above the melting point of Ti-5553, some Mo particles undergo partial dissolution during L-PBF (fig. S10, A and B, stages a and b). Mo has a very high melting point of 2783 K—much higher than the 1877 to 1933 K of the β-Ti phase in Ti-5553 (*43*)—and is thermodynamically quasi-stable in the titanium melt. Given the high reactivity of liquid titanium, such characteristics are essential to ensure that some solid Mo particles survive in the melt long enough for grain nucleation. During the laser melting process, the partial dissolution of Mo particles creates an enveloping liquid enriched in Mo solute (fig. S10, A and B, stage b). Although the Mo-rich solute in this enveloping liquid is expected to rapidly diffuse and mix with the bulk liquid, the continued dissolution (or melt-back)

of the particle provides a steady flux of Mo solute. The local Mo composition in this region may reach very high levels well beyond the nominal bulk alloy composition. The DICTRA simulation supports concentrations of ~20 wt % Mo extending a few micrometers into the melt; however, a very steep concentration gradient closer to the particle-liquid interface exists, so the local concentration may exceed this. The local Q and ΔT_{FR} values increase to ~18.5 K at 20 wt % Mo but would increase further with the concentration of Mo solute. This Mo-rich liquid surrounding the surviving solid Mo core may provide a supercooled zone if the temperature of the melt pool drops rapidly (fig. S10B, stages c and d). Although this supercooled zone arises as a result of localized composition variations, its generation is conceptually different from the traditional notion of constitutional supercooling, which develops as a result of the solute rejection into the melt ahead of a growing solid-liquid interface, thereby restricting the growth of the solid phase (*39*). In the current case, the surrounding enriched Mo solute has developed from Mo particle dissolution, creating a rich transient Ti-Mo liquid (richer in Mo compared with the nominal alloy

composition) that facilitates the development of a supercooled zone ahead of the particle as the melt temperature falls (fig. S10B, stages c and f). Consequently, the confluence of these factors and the presence of multiple Mo particles spatially distributed throughout the melt results in the fine equiaxed grain structure of Ti-55553+5Mo.

Constituent phases

In addition to refining the grain structure, the Mo addition also alters the constituent phases in the microstructure in the solid state. Although some of the larger Mo powders evidently survive to nucleate equiaxed grains, many of the smaller particles added are likely fully dissolved in the melt pool and therefore increase the overall Mo solute concentration in the Ti-5553 alloy [see (*30*) for particle size distribution]. This inevitably affects the phase stability and microstructural evolution. We show the phase distribution along the building direction of the Ti-5553 part (Fig. 5, A and C), and, as expected, there is a clear variation in the distribution of α phase from the bottom to the top of the part. The presence of α phase is further confirmed by x-ray diffraction (XRD) (Fig.

5B). The TEM selected-area electron diffraction (SAED) pattern in Fig. 1C has some discrete diffraction spots, which are the signature for the isothermal ω phase. This observation is consistent with the coexistence of the isothermal ω phase and the α phase in Ti-5553 upon being heat treated in the temperature range of 523 to 773 K (*44, 45*). Our differential scanning calorimeter (DSC) measurement further supports the formation of these phases in this temperature range (fig. S11). The addition of Mo tends to stabilize the β phase and suppress the precipitation of the α phase. We observed that the addition of Mo up to 5.0 wt % results in an intensity reduction of the α phase in the XRD spectra (Fig. 5B). Although other phases possibly may be present in Ti-5553+5Mo that we could not detect within the sensitivity of our XRD, if other phases do exist, they have no notable effect on the mechanical properties or uniformity. In contrast to Ti-5553, Ti-5553+5Mo shows solidification cellular structures along the building direction (Fig. 5, D and E) without any evidence of the needle-like α phase. Further SEM-EDX of the cellular structures reveals that the boundary (dark region) of the cellular structures is enriched in Ti solute (Fig. 5E and fig. S12).

This observation is expected when Ti is alloyed with β-isomorphous elements such as Ta, W, Nb, and Mo because these elements have partition coefficients greater than unity (*18*). The formation of cellular structures has also been reported in high-solute–containing alloys produced by L-PBF—for example, 316L stainless steel (*3*), Ni-based superalloy (*46*), and Ti–42Nb alloy (*47*)—and is commonly associated with the microsegregation of solute in solidification.

By promoting grain refinement during solidification and stabilizing the β phase under solid-state thermal cycling, the single, small Mo addition results in two notable changes in the mechanical property of Ti-5553: (i) a simultaneously improved yield strength and ductility and (ii) an enhanced uniformity in mechanical properties (Fig. 2A and table S2). The strength increase is attributed primarily to the combined effect of solid solution strengthening of Mo solute and grain refinement, based on the estimation of strengthening contributions (*30*) (fig. S16). Unlike the addition of β-eutectoid elements, which increase the strength at the expense of ductility (*48*), the Mo addition simultaneously enhances the strength and ductility.

The ductility improvement is mainly attributed to the suppression of precipitation of metastable phases by Mo solute as opposed to other potential effects, such as the transformation-induced plasticity effect (*30*). The coherent interface between the Mo particle and Ti alloy may not adversely affect the fatigue performance (*30*). Furthermore, the nanoparticles contribute to the high uniformity of mechanical properties of Ti-5553+5Mo because of their bifunctional role in the elimination of both textured columnar grain and phase heterogeneities. The primary aim of our design strategy is to demonstrate that we can eliminate the coexistence of columnar grains and phase heterogeneities through a single additive. Because we have not fully explored the compositional space, we do not know whether 5.0 wt % Mo is the optimal addition level, so further fine-tuning may lead to greater improvement in mechanical properties.

Conclusion

We explored how to simultaneously address the formation of columnar grains and heterogeneously distributed phases in the Ti-5553 alloy produced by L-PBF. We have shown that the
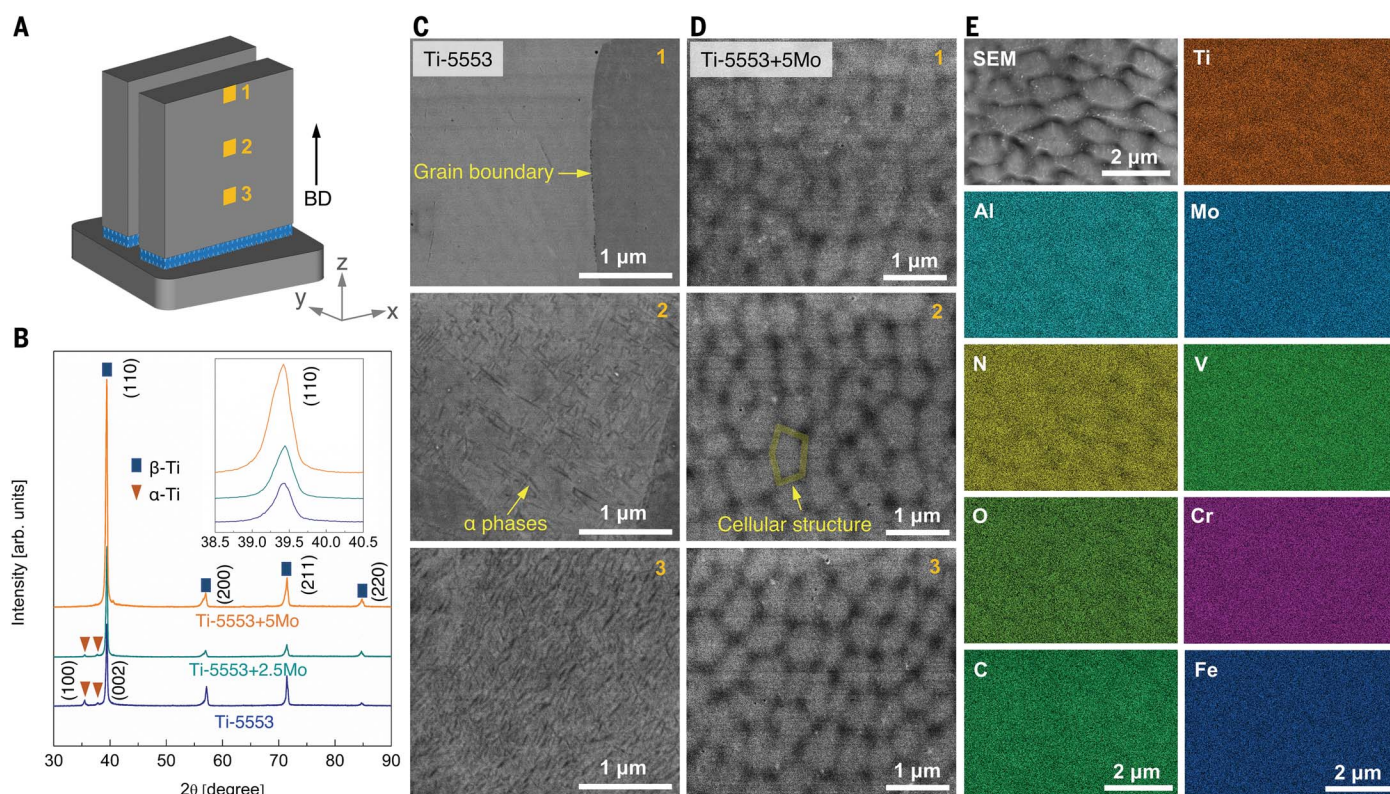

Fig. 5. Phase analysis of Ti-5553 and Mo-doped Ti-5553. (**A**) Schematic illustration showing microstructural examinations of different locations (1, 2, and 3) in a Ti-5553 cubic part. (**B**) XRD spectra showing the effect of Mo additions on the phase change. The inset shows the β(110) peak shifts toward lower angles. arb. units, arbitrary units. (**C**) SEM-BSE images showing the heterogeneous phase distribution along the building direction of the Ti-5553 part. The numbers in the upper right corners indicate the locations where the SEM-BSE was performed, as schematically illustrated in (A). These SEM-BSE images were taken using a concentric backscattered detector at a low accelerating voltage (3 kV) and a small working distance (6 mm). The phase contrast stems partially from electron channeling (*25*). (**D**) SEM-BSE images showing solidification cellular structures in Ti-5553+5Mo. The numbers indicate the locations where the SEM-BSE was performed, as schematically illustrated in (A). (**E**) SEM-EDX maps showing elemental segregation in cellular structures.

addition of Mo up to 5.0 wt % to Ti-5553 results in substantial CET and grain refinement, which we attributed to heterogeneous nucleation on partially unmelted Mo particles, with the dissolved Mo solute developing a supercooling zone that enhances the grain refinement efficiency. Additionally, the dissolved Mo solute enables the elimination of phase heterogeneities in Ti-5553 by stabilizing the β phase. Compared with Ti-5553, Ti-5553+5Mo exhibits higher strength, higher ductility, and more uniform tensile properties. More broadly, we anticipate that the design strategy is likely to be applicable beyond the titanium alloy considered here and could guide the design of other alloys because both columnar grains and heterogeneously distributed phases are frequently reported in a wide range of metallic alloys produced by 3D printing (*10, 23, 24, 49–52*).

REFERENCES AND NOTES

1. D. Herzog, V. Seyda, E. Wycisk, C. Emmelmann, *Acta Mater.* **117**, 371–392 (2016).
2. T. DebRoy *et al.*, *Prog. Mater. Sci.* **92**, 112–224 (2018).
3. Y. M. Wang *et al.*, *Nat. Mater.* **17**, 63–71 (2018).
4. R. Cunningham *et al.*, *Science* **363**, 849–852 (2019).
5. P. Kürnsteiner *et al.*, *Nature* **582**, 515–519 (2020).
6. C. Panwisawas, Y. T. Tang, R. C. Reed, *Nat. Commun.* **11**, 2327 (2020).
7. T. Zhang *et al.*, *Science* **374**, 478–482 (2021).
8. J. H. Martin *et al.*, *Nature* **549**, 365–369 (2017).
9. D. Zhang *et al.*, *Nature* **576**, 91–95 (2019).
10. T. M. Pollock, A. J. Clarke, S. S. Babu, *Metall. Mater. Trans. A* **51**, 6000–6019 (2020).
11. B. E. Carroll, T. A. Palmer, A. M. Beese, *Acta Mater.* **87**, 309–320 (2015).
12. T. DebRoy, T. Mukherjee, H. L. Wei, J. W. Elmer, J. O. Milewski, *Nat. Rev. Mater.* **6**, 48–68 (2021).
13. M. J. Bermingham, D. H. StJohn, J. Krynen, S. Tedman-Jones, M. S. Dargusch, *Acta Mater.* **168**, 261–274 (2019).
14. Q. Tan *et al.*, *Acta Mater.* **196**, 1–16 (2020).
15. Y. Liu *et al.*, *Acta Mater.* **220**, 117311 (2021).
16. P. Kontis *et al.*, *Acta Mater.* **177**, 209–221 (2019).
17. C. J. Todaro *et al.*, *Nat. Commun.* **11**, 142 (2020).
18. D. Zhang *et al.*, *Metall. Mater. Trans. A* **51**, 4341–4359 (2020).
19. M. M. Kirka, P. Nandwana, Y. Lee, R. Dehoff, *Scr. Mater.* **135**, 130–134 (2017).
20. W. Xu *et al.*, *Acta Mater.* **85**, 74–84 (2015).
21. T. Mukherjee, T. DebRoy, T. J. Lienert, S. A. Maloy, P. Hosemann, *Acta Mater.* **209**, 116775 (2021).
22. J. Zhang *et al.*, *Nat. Commun.* **13**, 4660 (2022).
23. P. C. Collins, D. A. Brice, P. Samimi, I. Ghamarian, H. L. Fraser, *Annu. Rev. Mater. Res.* **46**, 63–91 (2016).
24. J. J. Lewandowski, M. Seifi, *Annu. Rev. Mater. Res.* **46**, 151–186 (2016).
25. J. Haubrich *et al.*, *Acta Mater.* **167**, 136–148 (2019).
26. M. Laleh *et al.*, *Prog. Mater. Sci.* **133**, 101051 (2023).
27. C. Hicks, G. Sivaswamy, T. Konkova, P. Blackwell, *Mater. Sci. Eng. A* **825**, 141928 (2021).
28. A. Caballero *et al.*, *Philos. Mag.* **102**, 2256–2281 (2022).
29. J. Zhang, M. Bermingham, J. Otte, Y. Liu, M. Dargusch, *Scr. Mater.* **223**, 115066 (2023).
30. Materials and methods are available as supplementary materials.
31. H. Kumar, P. Kumar, W. Y. Yeong, R. L. Narayan, U. Ramamurty, *Acta Mater.* **225**, 117593 (2022).
32. H. Deng *et al.*, *J. Alloys Compd.* **810**, 151792 (2019).
33. Z. Liu *et al.*, *Mater. Sci. Eng. A* **798**, 140093 (2020).
34. A. Zafari, E. W. C. Lui, M. Li, K. Xia, *J. Mater. Sci. Technol.* **105**, 131–141 (2022).
35. H. Schwab, F. Palm, U. Kühn, J. Eckert, *Mater. Des.* **105**, 75–80 (2016).
36. H. D. Carlton, K. D. Klein, J. W. Elmer, *Sci. Technol. Weld. Join.* **24**, 465–473 (2019).
37. T. Zhang *et al.*, *Mater. Sci. Eng. A* **835**, 142624 (2022).
38. B. He, J. Li, X. Cheng, H.-M. Wang, *Mater. Sci. Eng. A* **699**, 229–238 (2017).
39. D. H. StJohn, M. Qian, M. A. Easton, P. Cao, *Acta Mater.* **59**, 4907–4921 (2011).
40. M. J. Bermingham, D. Kent, H. Zhan, D. H. Stjohn, M. S. Dargusch, *Acta Mater.* **91**, 289–303 (2015).
41. M. A. Easton, D. H. StJohn, *Acta Mater.* **49**, 1867–1878 (2001).
42. M. S. K. K. Y. Nartu *et al.*, *Nat. Commun.* **14**, 3288 (2023).
43. C. Leyens, M. Peters, Eds., *Titanium and Titanium Alloys: Fundamentals and Applications* (Wiley, 2005).
44. N. G. Jones, R. J. Dashwood, M. Jackson, D. Dye, *Acta Mater.* **57**, 3830–3839 (2009).
45. Y. Zheng *et al.*, *Acta Mater.* **103**, 850–858 (2016).
46. T. Keller *et al.*, *Acta Mater.* **139**, 244–253 (2017).
47. S. Tekumalla, M. Seita, S. Zaefferer, *Acta Mater.* **262**, 119413 (2024).
48. Z. Xiong, X. Pang, S. Liu, Z. Li, R. D. K. Misra, *Scr. Mater.* **195**, 113727 (2021).
49. S. A. Mantri, R. Banerjee, *Addit. Manuf.* **23**, 86–98 (2018).
50. M. Duport *et al.*, *Addit. Manuf.* **61**, 103340 (2023).
51. Y. Tian *et al.*, *Metall. Mater. Trans. A* **45**, 4470–4483 (2014).
52. S. H. Sun *et al.*, *Acta Mater.* **64**, 154–168 (2014).
53. J. Zhang *et al.*, Data from: Ultra-uniform, strong and ductile 3D printed titanium alloy through bifunctional alloy design, dataset, *Dryad* (2024); https://datadryad.org/stash/dataset/doi:10.5061/dryad.6t1g1jx50.

SUPPLEMENTARY MATERIALS

science.org/doi/10.1126/science.adj0141
Materials and Methods
Supplementary Text
Figs. S1 to S18
Tables S1 to S5
References (*54–73*)